TU Delft

Delft University of Technology

Document Version
Final published version

Licence
CC BY

Citation (APA)
van Nierop, N. D., & Jongbloed, B. C. P. (2026). Introducing a novel combined power-amplitude control method for continuous ultrasonic welding of CF/LMPAEK composites. *Journal of Advanced Joining Processes*, *14*, Article 100423. https://doi.org/10.1016/j.jajp.2026.100423

Important note
To cite this publication, please use the final published version (if applicable).
Please check the document version above.

Copyright
In case the licence states “Dutch Copyright Act (Article 25fa)”, this publication was made available Green Open Access via the TU Delft Institutional Repository pursuant to Dutch Copyright Act (Article 25fa, the Taverne amendment). This provision does not affect copyright ownership.
Unless copyright is transferred by contract or statute, it remains with the copyright holder.

Sharing and reuse
Other than for strictly personal use, it is not permitted to download, forward or distribute the text or part of it, without the consent of the author(s) and/or copyright holder(s), unless the work is under an open content license such as Creative Commons.

Takedown policy
Please contact us and provide details if you believe this document breaches copyrights.
We will remove access to the work immediately and investigate your claim.

This work is downloaded from Delft University of Technology.

Journal of Advanced Joining Processes 14 (2026) 100423

Contents lists available at ScienceDirect

Journal of Advanced Joining Processes

journal homepage: www.sciencedirect.com/journal/journal-of-advanced-joining-processes

Introducing a novel combined power-amplitude control method for continuous ultrasonic welding of CF/LMPAEK composites

Nigel van Nierop, Bram Jongbloed *

SAM XL, TU Delft Campus, Rotterdamseweg 382C, 2629 HG, Delft, The Netherlands
Intelligent Manufacturing Systems, Department of Aerospace Structures and Materials, Faculty of Aerospace Engineering, Delft University of Technology, Kluyverweg 1, 2629 HS, Delft, The Netherlands

ARTICLE INFO

Keywords:
Continuous ultrasonic welding
CFRP
Process control
Thermoplastic composite
Joining
Assembly

ABSTRACT

The increasing demands for high production rates, reduced costs, and more sustainable aircraft structures encourage the rapid introduction of thermoplastic composites in aerospace applications. A major challenge for their widespread implementation, especially in single-aisle aircraft programs, lies in meeting the required high production rates of up to 80–100 aircraft per month. Fast, automated manufacturing technologies such as thermoforming and welding are therefore essential to enable scalable industrialization. Continuous ultrasonic welding is such a high-speed joining technique. However, for stiff aerospace-grade composites, it remains challenging to achieve uniformly welded seams using current state-of-the-art control methods. This study investigated the potential for improving process robustness and weld quality in continuous ultrasonic welding of CF/LMPAEK adherends made from unidirectional plies by introducing a novel combined power-amplitude control method. Welds were produced using the state-of-the-art constant-amplitude and constant-power control methods, as well as the newly introduced approach, and were compared in terms of power and amplitude responses, heating uniformity, and resulting weld quality. A combined fuzzy power-amplitude control method was developed and implemented. Under the processing conditions investigated in this study, the proposed control method reduced extreme fluctuations in power and amplitude and was associated with improvements in weld strength and weld uniformity. Overall, the findings indicate that combined power-amplitude control is a promising approach for improving the robustness and quality of continuous ultrasonic welding of thermoplastic composites.

Introduction

In the aviation industry, increasing demands for high production rates, reduced costs, and more sustainable aircraft encourage the accelerated introduction of lightweight thermoplastic composites in aircraft structures. These high production rates are particularly applicable for next-generation single-aisle aircraft. In contrast to thermoset composites, thermoplastic composites can be re-molten and re-shaped after initial consolidation. This processability enables high-speed manufacturing technologies, such as thermoforming for part production and assembly using welding technologies, resulting in cost-effective solutions. Additionally, due to their re-processability, thermoplastic composites are inherently more recyclable than thermoset composites.

Various welding techniques exist for thermoplastic composites: ultrasonic, infrared, conduction, resistance, and induction welding technologies (Costa et al., 2012; Yuan et al., 2026; Fernandez Villegas et al., 2013; Larsen et al., 2025; Liu et al., 2025). Resistance welding has been used for the assembly of ribs in the fixed leading edge of A380 (Gardiner, 2006), and induction welding has been used for the assembly of the tail section in the Gulfstream G650 (Offringa, 2010) and for the fuel tank access cover in A220. Of the aforementioned welding technologies, continuous ultrasonic welding stands out when it comes to welding speed (Gardiner, 2022; Fernandez Villegas et al., 2013; Senders et al., 2016), especially when long seams are required, such as the welding of stiffeners to a skin (Larsen et al., 2025). Additionally, the process is considered energy-efficient, because heat is generated mainly at the welding interface and because of the high speed there is little time for heat to transfer away to the surroundings.

In ultrasonic welding of thermoplastic composites, the ultrasonic welder applies high-frequency (typically 20 kHz), low amplitude (typically 30–100 μm peak-to-peak) mechanical vibrations to the composite

* Corresponding author at: Intelligent Manufacturing Systems, Department of Aerospace Structures and Materials, Faculty of Aerospace Engineering, Delft University of Technology, Kluyverweg 1, 2629 HS, Delft, The Netherlands.
E-mail address: B.C.P.Jongbloed@tudelft.nl (B. Jongbloed).

https://doi.org/10.1016/j.jajp.2026.100423
Received 27 May 2026; Received in revised form 9 July 2026; Accepted 29 July 2026
Available online 3 August 2026
2666-3309/© 2026 The Authors. Published by Elsevier B.V. This is an open access article under the CC BY license (http://creativecommons.org/licenses/by/4.0/).

parts through a sonotrode, while applying a static welding force with the same sonotrode. An energy director (ED) made from either a polymer film (Fernandez Villegas, 2015; Palardy and Fernandez Villegas, 2017; Senders et al., 2016) or mesh (Jongbloed et al., 2020b) is placed in between the to-be-welded composite parts, hereafter referred to as adherends, to focus the heat generation at the weld interface. The ED is usually made of thermoplastic resin of the same material as the composite matrix material. The mechanical vibrations cause frictional heating between the surfaces of the ED and the adherends and viscoelastic heating (Potente, 1984; Zhang et al., 2010). The heating rate due to viscoelastic friction occurs according to the following equation (Benatar and Gutowski, 1989):

$$\dot{Q}_v = \frac{\omega E'' \varepsilon^2}{2} \tag{1}$$

where ω is the vibration frequency, E'' is the material loss modulus, and ε is the cyclic strain undergone by the material as a result of the mechanical vibrations. Due to the lower compressive stiffness, the ED undergoes a higher compressive straining than the adherends and consequently experiences higher heating rates than the adherends (Benatar et al., 1989; Fernandez Villegas, 2019). Two ultrasonic welding processes can be distinguished: static welding and continuous welding. In static welding, the sonotrode remains stationary with respect to the adherends, providing both the vibrations for heating and the subsequent force for consolidation after stopping the vibrations (Fernandez Villegas, 2014; Zhao et al., 2017; Choudhary et al., 2026). In continuous ultrasonic welding (CUW), the sonotrode moves relative to the adherends while continuously applying a welding force and the mechanical vibrations, followed by a consolidator that ensures cooling under pressure to prevent deconsolidation (Jongbloed et al., 2022). In contrast to static welding, continuous ultrasonic welding makes it possible to make long fluid-tight seams, giving significant advantages over spot welding, and as such, the application of the two technologies will be different, e.g., static spot welding for clips, brackets, and CUW for long seams for longitudinal joints or stiffeners. Jongbloed et al. recently introduced a rounded sonotrode, which also makes circumferential welding possible in a continuous fashion while having the advantage of having lower maximum temperatures at the welding interface as compared to the traditional rectangular sonotrode with a flat contacting surface (Jongbloed et al., 2023).

For continuous ultrasonic welding, research into effective weld control methods has been limited. Typically, constant amplitude control has been used in various studies (Senders et al., 2016; Jongbloed et al., 2020b,a, 2021, 2022, 2023; Köhler et al., 2024). For the ultrasonic welding generator to achieve the set constant amplitude during the entire welding process, the power fluctuates as a result of changes in the mechanical impedance under the sonotrode (Benatar and Gutowski, 1989). The constant amplitude control method seems to work well for welding of fabric-based adherends as shown in Jongbloed et al. (2020b, 2022, 2020a, 2021, 2023) and Senders et al. (2016). However, it is more challenging to obtain high quality welded seams, i.e. high strength and low variation over weld length with high weld uniformity, when the same control method is used for welding adherends made from unidirectional (UD) plies. For UD-based CF/LMPAEK (carbon fiber/Low-Melt Polyaryletherketone) adherends, the relatively high scatter in strength over the length of a weld together with the reduced weld uniformity and thus the increased presence of unwelded and overwelded areas as observed in Köhler et al. (2024) and Janek et al. (2025) indicates an alternative control method might be required.

As an alternative to constant amplitude welding, Janek et al. recently introduced constant power welding as an attempt to improve the weld control method (Janek et al., 2025). In constant power welding, the power draw is kept constant, and consequently, the vibration amplitude fluctuates during welding. They found that constant power control is more agile and sensitive, which helped initiate the weld seam in their tested configurations, and aided in restoring weld quality after declines in strength caused by their clamping method. However, they concluded that the constant amplitude control method is more robust, leading to a more uniform weld quality when the overall process conditions are unstable or metastable. The constant power control method seems to work well under stable welding conditions that result in low fluctuations in generator output power. They concluded that likely pure constant power control is unsuitable for industrial applications where tolerances, material variability, and changes in boundary conditions are present.

Therefore, with the aim of understanding how to improve the process robustness and weld quality for welding of CF/LMPAEK adherends consisting of unidirectional plies, the present study introduces a novel control method referred to as combined power-amplitude control. In this study, this novel method is methodically compared with the state-of-the-art constant amplitude and constant power control methods. The welds produced using these three control methods are evaluated based on their power and amplitude responses, heating uniformity, and resulting weld quality including lap shear strength and weld uniformity. Additionally, correlations between the power and amplitude data and the observed weld quality are analyzed to understand how the control methods influence weld quality.

Methodology

Materials

The thermoplastic composite material used in this study was CF/LMPAEK (carbon fiber/Low-Melt Polyaryletherketone) of Toray Cetex® TC1225. Toray Advanced Composites supplied consolidated laminates measuring 1800 mm × 1200 mm. Multiple laminates were provided for welding experiments; these consisted of 12 unidirectional plies with a lay-up sequence of [45/0/135/0/90/0/0/90/0/135/0/45]. In addition, a one-shot consolidated reference laminate was provided, comprising 24 unidirectional plies with a lay-up of [45/0/135/0/90/0/90/0/135/0/45]s. No defects were visible on the c-scans performed by Toray for any of these laminates. From these laminates, adherends of dimensions 500 mm × 106.25 mm were cut using a water-cooled diamond saw, a Compcut ACS 600, by Compcut Advanced Composite Machining. This resulted in edges free of delaminations. Before welding, the adherends were dried in an oven at 120 °C for 24 h to exclude the effect of moisture in the material from this study. Immediately prior to welding, the adherends were cleaned with isopropyl alcohol and then arranged in a single-lap shear configuration with an overlap of 30 mm. Note that in contrast to most research on welding of CF/LMPAEK (Köhler et al., 2024; Janek et al., 2025) where an overlap of 12.7 mm is chosen in agreement with ASTM D1002, in the current study a much wider overlap of 30 mm was chosen to have a weld width realistically representing the width of a stiffener foot similar to those in the STUNNING project within the MFFD (Multifunctional Fuselage Demonstrator) (van Dooren and Bisagni, 2023). Additionally, an energy director of 500 μm-thick was used in the form of an expanded mesh made from a LMPAEK film supplied by Toray, with an areal weight of approximately 240 gsm. This mesh thickness was chosen in this study because it is known from previous studies to be suitable for continuous ultrasonic welding (Asnani, 2025; van Stuyvesant Meijen and Jongbloed, 2025). In our study, this mesh resulted in an effective weld line thickness of approximately 0.26 mm.

Welding setup and welding process

Welding experiments were performed using the SAM XL robotic continuous ultrasonic welding setup, shown in Fig. 1(a). The system consists of a KUKA KR560 R3100-2 industrial robot mounted on a custom 2.0 m-long Vansichen track for welding motion, and an in-house-developed continuous ultrasonic welding end-effector (EEF).

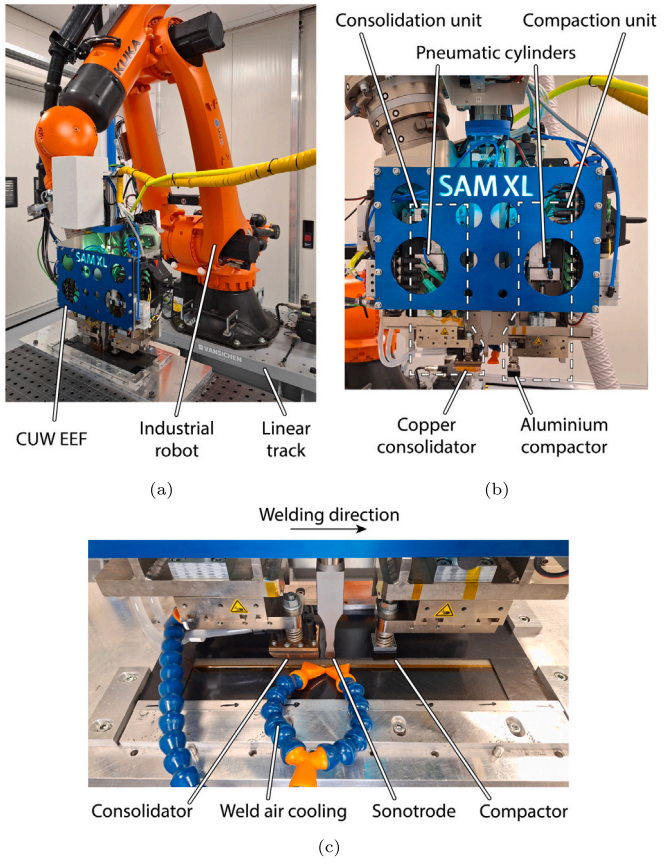


Fig. 1. Overview of the robotic continuous ultrasonic welding setup at SAM XL showing (a) an industrial robot with the CUW end-effector, (b) a close-up of the end-effector, and (c) a close-up of the consolidator, sonotrode, and compactor in their deployed welding configuration.

The EEF is equipped with its own industrial controller (cRIO-9039 CompactRIO Controller) and a PC running LabVIEW for data logging.

The end-effector is shown in Figs. 1(a) and 1(b), and in its deployed welding configuration in Fig. 1(c). It consists of a rigid enclosure housing an integrated ultrasonic welding system supplied by Herrmann Ultrasonics, along with a consolidation unit, a compaction unit, and an air cooling system. The integrated ultrasonic welding system comprises a 20 kHz ULTRABOND 48.20 G7 digital ultrasonic generator, electrically coupled to a welding stack consisting of a piezoelectric converter, a steel booster, and a steel sonotrode. Additionally, a VE20 SLIMLINE DIALOG 6200 system is used for welding force application.

A rounded sonotrode (Jongbloed et al., 2023) was custom-manufactured by Herrmann Ultrasonics; its radius of 17.5 mm and width of 30 mm were specified, whereas all other components were off-the-shelf. To enable digital communication with the ultrasonic generator, an ULTRA-X fieldbus EtherCAT module was installed by Herrmann Ultrasonics in both the ULTRABOND generator and the VE20 SLIMLINE DIALOG 6200 system. Herrmann Ultrasonics provided operational manuals detailing communication with the ultrasonic generator, external control via the EtherCAT protocol, and access to internal registers.

The converter outputs a range of peak-to-peak amplitudes that scale linearly with the generator amplitude setpoint, with a continuous maximum of 25 μm at 100% generator amplitude. For short durations, the generator can exceed this limit up to a theoretical maximum of 130%. The output amplitude of the converter is amplified by the gain factors of the booster and sonotrode, which are 1.5 and 2.4, respectively, resulting in a sonotrode peak-to-peak vibration amplitude of 90 μm at 100% generator amplitude. The sonotrode applied a welding force of 1800 N. This force is higher than the 1000 N previously reported for a 12.7 mm overlap (Jongbloed et al., 2023), to achieve a comparable welding pressure for the larger overlap width considered in the present study.

Downstream of the sonotrode, an actively water-cooled copper consolidator (CuCr1Zr alloy) was used to cool the weld while applying a consolidation pressure of 1.8 MPa over a contact area of 40 mm × 30 mm, as illustrated in Fig. 2. The cooling system is shown in Fig. 3, and continuously circulated demineralized water using a pump (EK-Quantum Kinetic TBE 160 DDC PWM) operating at maximum flow rate. The water entered the consolidator from the front, exited at the back, passed through a radiator (Corsair Hydro X Series XR5 360 mm), and returned to the consolidator. The cooling system maintained the consolidator temperature between 20 °C and 45 °C without requiring a PI controller for flow regulation, as also reported in Jongbloed et al. (2024). The consolidator temperature was monitored in real time for all welds using a type K thermocouple mounted on the consolidator. The consolidator was positioned such that the nearest point of its contact area was 11 mm from the sonotrode center in the welding direction, as illustrated in Fig. 2.

Upstream of the sonotrode, an anodized aluminium compaction block ensured that the adherends were pressed together with a force of 1000 N over an area of 26 mm × 32 mm prior to interaction with the sonotrode. The contact area was centered relative to the sonotrode (Fig. 2). The compactor was positioned such that the nearest point of its contact area was 59 mm from the sonotrode center in the welding direction. The welding stack, consolidator, and compactor were actuated by pneumatic cylinders from Festo, which actively controlled the required forces. External air cooling was used to cool the top adherend near the sonotrode during welding, as shown in Fig. 1(c). The system consisted of a pressurized air supply at 8 bar and a 1/2″ Loc-Line cooling hose split into two outlets, both directed at the free edge of the top adherend, positioned 3 cm from the edge, and centered around the sonotrode.

Control and communication architecture

The communication flowchart of the complete robotic welding system is shown in Fig. 4. The system uses the EtherCAT communication protocol. Control of the entire welding end-effector is implemented in LabVIEW, running on the cRIO-9039 industrial controller. A human–machine interface (HMI) for end-effector control can be accessed on the PC, which is also used for data logging. The PC communicates with the cRIO via a dedicated Ethernet connection.

On the KUKA controller, dedicated welding programs were developed using the KRL programming language to ensure correct welding motion and synchronized activation and deactivation of process operations, such as turning the ultrasonic vibrations on and off and controlling the start and end of the weld. These welding programs can be executed via the robot controller using the teach pendant.

Data acquisition and synchronization

Table 1 summarizes the data acquisition framework used during the welding experiments. Kinematic process variables, including end-effector position and rotations, as well as welding speed, were recorded via the KUKA controller. Process-related signals, such as vibrational amplitude and consumed generator power, were directly acquired from the internal registers of the ULTRABOND ultrasonic welding generator. The welding force was obtained from the internal registers of the DIALOG 6200 system, whereas consolidation and compaction forces were measured using a Beckhoff-based system. In addition, the consolidator temperature was measured using a Beckhoff thermocouple system. All signals were transmitted to and synchronized on the cRIO-9039 real-time controller. The synchronized data were subsequently captured and stored by the data logging PC, enabling comprehensive monitoring and subsequent analysis of the welding process.

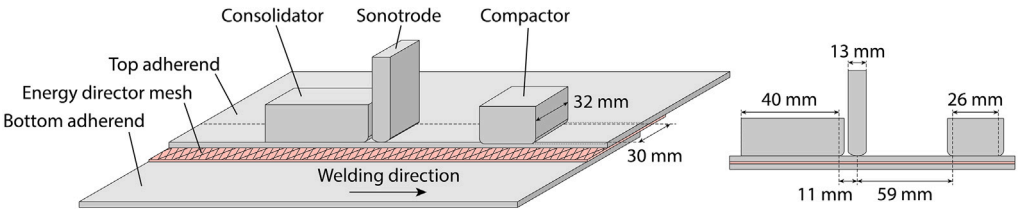


Fig. 2. Simplified schematic of the continuous ultrasonic welding configuration, showing the consolidator, sonotrode, and compactor (left) and their main dimensions and relative distances (right). Note: this figure is not to scale.

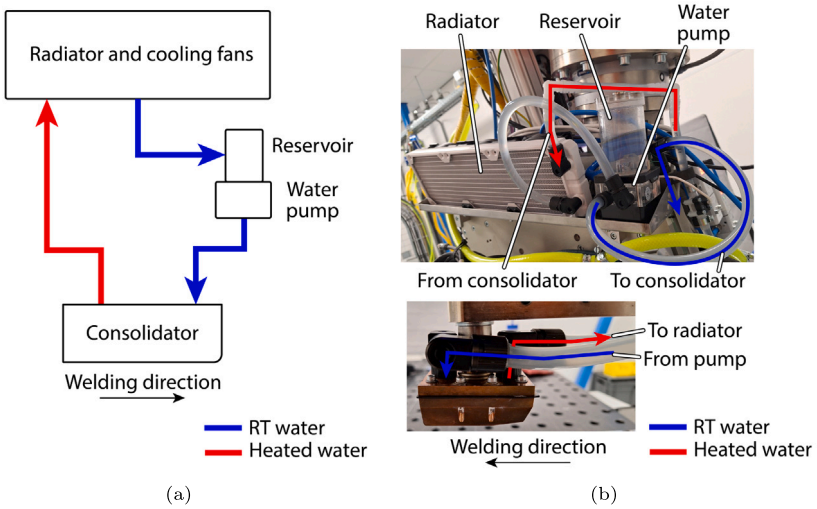


Fig. 3. Overview of the consolidator water cooling setup, with (a) a schematic and (b) the components as seen from the back of the end-effector. "RT water" is short for room temperature water.

Table 1
Overview of logged process variables, measurement units, sampling frequencies, and data sources.

Variable	Unit	Sampling rate [Hz]	Source
End effector position (X, Y, Z)	mm	245	KUKA controller
End effector rotations (R_x, R_y, R_z)	deg	245	KUKA controller
Welding speed	mm/s	245	KUKA controller
Vibrational amplitude	%	425	ULTRABOND generator
Consumed generator power	W	425	ULTRABOND generator
Welding force	N	250	DIALOG 6200
Consolidation force	N	200	Beckhoff system
Compaction force	N	200	Beckhoff system
Consolidator temperature	°C	50	Beckhoff thermocouple system

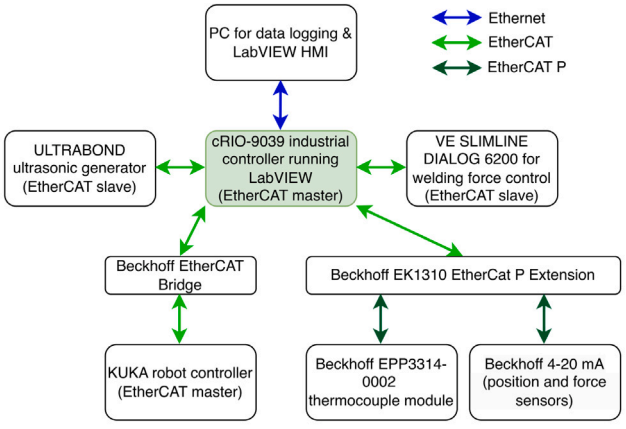


Fig. 4. Schematic showing the communication structure of the continuous ultrasonic welding setup.

Adherend clamping conditions

During welding, the adherends were constrained using a picture frame jig (Fig. 5(a)). A weld overlap of 30 mm was used, as shown in the schematic cross-sectional front view (Fig. 5(b)). The ED was kept in place using Kapton tape parallel to the welding direction. Since the picture frame constraints allow for movement of the adherends perpendicular to the welding direction, the bottom adherend was taped to the picture frame, and spacer plates were used to constrain the top adherend from moving in this direction. This clamping approach aimed to provide a free movement of the top adherend in the out-of-plane direction to minimize the effect of the clamping on the joint quality (B. G. Brito et al., 2022). A support plate of the same material and thickness as the adherends was placed below the top adherend to prevent rotation in the jig prior to welding. This did not affect the welding process, as the applied forces during welding held the top adherend horizontal, thereby preventing contact with the support plate. The welding was performed from 80 to 420 mm of the total 500 mm adherend length as shown in Fig. 6, to accommodate space for the consolidator and compactor on the top adherend outside the weld zone.

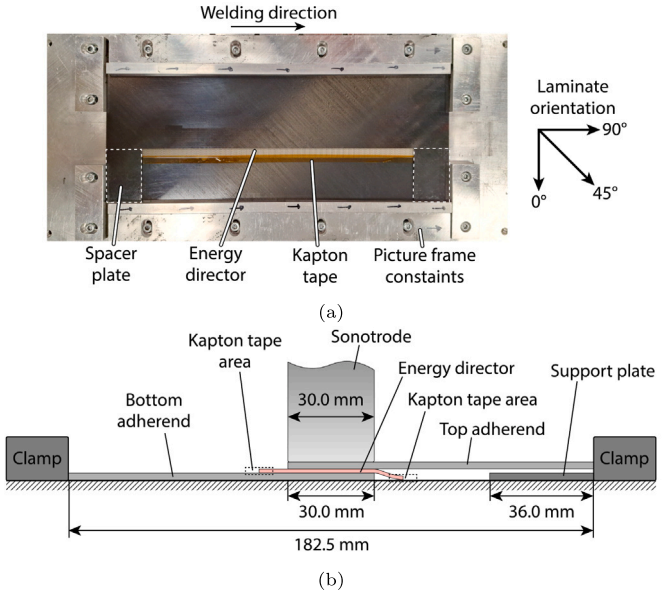


Fig. 5. Overview of the clamping configuration used during welding, including (a) the picture frame jig, and (b) the cross-sectional front view of the welding configuration, not to scale.

This is an alternative method to using run-on and run-off laminates as shown in Jongbloed et al. (2022). The same schematic also indicates the locations of the test coupons T1 to T9.

In-situ thermographic monitoring

Thermography images of the top surface temperature of the welded area after consolidation were created using a FLIR A655sc thermal camera with a 25-degree field-of-view lens. The camera was mounted to the end-effector and positioned to view the region behind the consolidator, as shown in Fig. 7. During welding, temperature data were recorded over the complete camera viewing area. In post-processing, the captured column of temperature pixel data at a distance of 75 mm behind the sonotrode center was extracted from each frame. This distance was the closest at which the weld width was fully visible and no longer obstructed by the consolidator. The thermography images in this study were then created by using the timestamps of the data to place it at the correct location along the adherend length, and at the correct location over the weld width by calibrating the camera orientation in space.

From the thermography images, the average and standard deviation of the top surface temperature after consolidation were calculated. To compute these statistics, the data was used from the start of coupon T1 to the end of coupon T9 as indicated in Fig. 6. To eliminate any effects due to calibration inaccuracies and potentially cooler edges resulting from air cooling, a margin of 3 mm was excluded from both longitudinal weld edges.

Weld control implementation

In this study, three control methods were used: constant amplitude, constant power, and combined power-amplitude control. The control diagrams of their implementation are shown in Fig. 8. For all methods, either a single amplitude setpoint or a continuous real-time stream of amplitude setpoints is transmitted via the EtherCAT communication protocol to the Herrmann ultrasonic generator. The internal amplitude controller of the ultrasonic generator then ensures that the output amplitude accurately follows the commanded setpoint.

For constant amplitude control, a single amplitude setpoint (S_a) is sent prior to welding and remains unchanged ($S_a = A$, with A being the amplitude requested from the ultrasonic generator in %), since no outer feedback loop is used (see Fig. 8(a)). For the other two control methods, a cascaded control structure is employed, in which either a power setpoint (S_p) alone or a combination of power (S_p) and amplitude setpoints (S_a) is used. For both methods, a continuous stream of requested amplitudes (A) is generated in real time by an in-house-developed controller running on the cRIO and is sent to the internal controller of the Herrmann ultrasonic generator at a rate of approximately 425 Hz. For all three control methods, C_a and C_p represent the real-time vibrational amplitude [%] and consumed power [W], respectively, as provided by the internal registers of the Herrmann generator.

Constant power control aims to regulate the power measured by the ultrasonic generator to the user-defined setpoint (S_p) by adjusting the requested amplitude (A). The control diagram for this method is shown in Fig. 8(b). Since power is controlled through amplitude, a correction is included for the assumption of $P \propto A^2$. The following control law is implemented in the outer-loop of the cRIO controller, with $dA = dA_{\mathrm{CP}}$:

$$A_{i+1} = \mathrm{clamp}\left(A_i + dt \cdot dA,\ A_{\min},\ A_{\max}\right) \tag{2}$$

$$dA_{\mathrm{CP}} = R \cdot \mathrm{sat}\left(\frac{e_{p,\sqrt{}}}{\sqrt{S_p + B_p} - \sqrt{S_p}},\ I_p\right) \tag{3}$$

$$e_{p,\sqrt{}} = \sqrt{S_p} - \sqrt{C_p} \tag{4}$$

$$\mathrm{sat}(x,\ I) = \begin{cases} -1, & x \le -1 \\ \frac{x}{I}, & -1 < x < 1 \\ 1, & x \ge 1, \end{cases} \qquad \mathrm{clamp}(x,\ a,\ b) = \begin{cases} a, & x \le a \\ x, & a < x < b \\ b, & x \ge b \end{cases} \tag{5}$$

where the subscript i denotes the discrete time index. Furthermore, A is the amplitude request sent to the ultrasonic generator (%), dt the timestep (ms), dA the control response (%/ms), A_{min} the minimum amplitude (%), A_{max} the maximum amplitude (%), R the maximum allowed response (%/ms), $e_{p,\sqrt{}}$ the transformed power error ($W^{1/2}$), S_p the power setpoint (W), C_p the measured power (W), B_p the power proportional band (W), and I_p a power response scaling factor (-).

The combined power-amplitude control method does not keep any variable constant, but instead allows both amplitude and power to fluctuate around their respective setpoints (S_a and/or S_p). It uses feedback from both the measured power and amplitude of the ultrasonic generator, as shown in Fig. 8(c). These signals are combined using fuzzy control logic, which assigns degree of membership fractions to the amplitude- and power-based contributions according to the measured amplitude error relative to the setpoint. These fractions sum to one, and an example of the corresponding limits is shown in Fig. 9. For an amplitude error between x_2 and x_3, the control method effectively operates in constant power mode, whereas outside x_1 and x_4, the control method operates in constant amplitude mode, with a continuous linear transition between these two regions. The new requested amplitude is computed using the same control law in Eq. (2), implemented in the outer-loop cRIO controller, with $dA = dA_{\mathrm{PA}}$:

$$dA_{\mathrm{PA}} = R \cdot \left(\mu_a \cdot \mathrm{sat}\left(\frac{e_a}{B_a},\ I_a\right) + \mu_p \cdot \mathrm{sat}\left(\frac{e_{p,\sqrt{}}}{\sqrt{S_p + B_p} - \sqrt{S_p}},\ I_p\right)\right) \tag{6}$$

$$e_a = S_a - C_a \tag{7}$$

where μ_a is the degree of membership of the amplitude feedback (-), μ_p is the degree of membership of the power feedback (-), e_a the amplitude error (%), S_a the amplitude setpoint (%), C_a the measured amplitude (%), B_a the amplitude proportional band (%), and I_a an amplitude response scaling factor (–).

These control methods have the following characteristics. First, the output is rate-limited to a maximum change of $dt \cdot R$, as the remaining

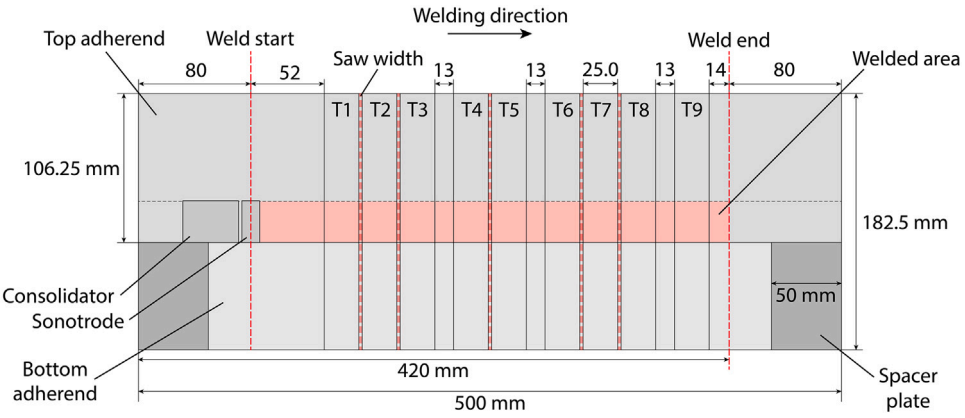


Fig. 6. Overview of how the coupons (T1-T9) for mechanical testing were extracted from welds. Dimensions are in mm, the saw width being 2 mm.

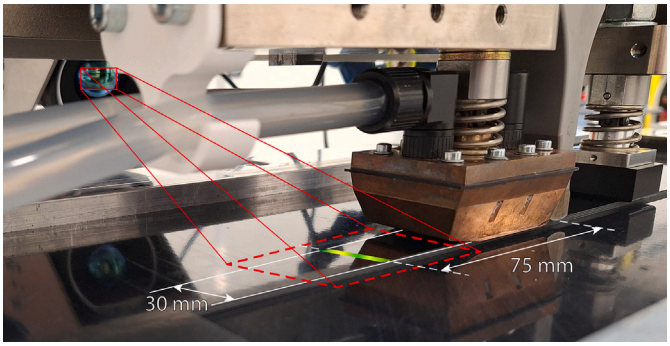


Fig. 7. Representation of the FLIR thermal camera mounted on the end-effector during welding.

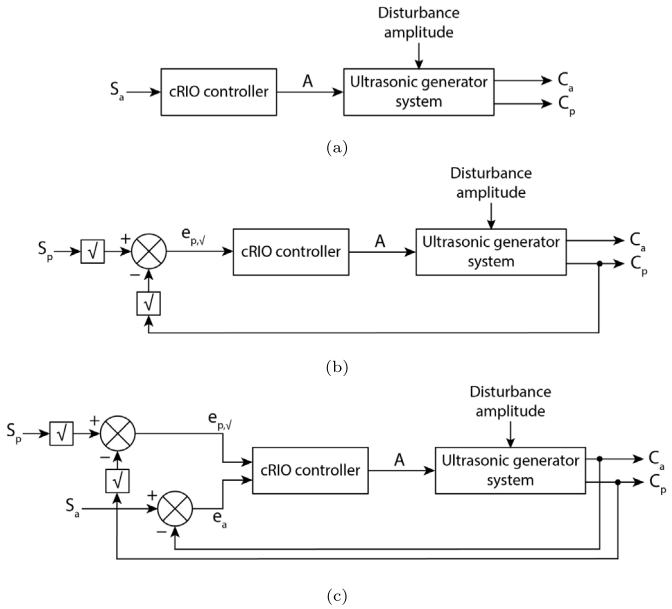


Fig. 8. Control diagrams for (a) constant amplitude control using the generator's internal amplitude controller; (b) constant power control with a cascading control method; and (c) combined power-amplitude control with a cascading fuzzy logic control method.

factor in the expression is bounded within the range [−1, 1]. This ensures that the ultrasonic generator amplitude controller can follow the commanded change for a timestep corresponding to the design

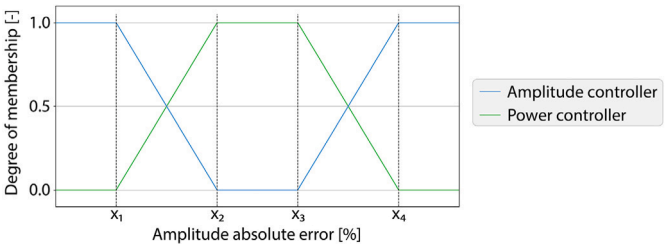


Fig. 9. Definition of the fuzzy control logic limits. x_1, x_2, x_3, and x_4 are the absolute amplitude error percentages in ascending order. In this figure symmetrical limits are shown where $x_1 = -x_2$ and $x_3 = -x_4$, but it can be made asymmetric.

control frequency of 425 Hz, provided that no significant timing irregularities occur. This was confirmed from logged data, which showed that the generator accurately followed the commanded amplitude. Second, the output amplitude setpoint is constrained between a minimum and maximum value, A_{min} and A_{max}. This acts as an anti-windup mechanism by preventing the setpoint from exceeding values that the generator can achieve. Additionally, this can be used to cap the amplitude at a specified value.

Process parameters and test matrix

The test matrix is presented in Table 2. For constant amplitude control, a vibration amplitude of 89% was used, corresponding to a peak-to-peak amplitude of 80 μm, which is known to be suitable for welding thermoplastic composites using a rounded sonotrode (Jongbloed et al., 2023). Based on initial experiments, the welding speed was set to 10 mm/s, which was found to be effective at the selected vibration amplitude. The same welding speed was subsequently used for all experiments in this study. For constant power control, a power setpoint of 1380 W was used. This setpoint was based on the average power observed during the constant amplitude welds over the full weld length, computed as 1383 W from weld start to weld end (see Fig. 6) and rounded to 1380 W. This ensured a comparable overall energy input between constant amplitude and constant power control. The average power was computed by integrating the power curve to obtain the total energy, which was then divided by the total weld duration. No additional constant-power setpoints were investigated.

In this study, two sets of combined power-amplitude control parameters were used: a symmetric version and an asymmetric version. The symmetric version was used as a preliminary experiment to tune the control parameters. The asymmetric version was developed following observations from the symmetric version and other tuning experiments,

Table 2
Experimental test matrix presenting the controller parameters for the different control methods.

Control method	Abbr.	No. of welds [–]	S_a [%]	S_p [W]	Controller parameters
Constant amplitude	CA	5	89	N/A	[–]
Constant power	CP	5	N/A	1380	R = 0.50%/ms, B_p = 150 W, I_p = 5, A_{min} = 15%, A_{max} = 127%
Power-amplitude	PA-sym	1	89	1380	Symmetric control response: R = 0.10%/ms, B_a = 6%, I_a = 1, B_p = 630 W, I_p = 1, $[x_1, x_2, x_3, x_4]$ = [−12, 0, 0, 12]%, A_{min} = 15%, A_{max} = 127%
Power-amplitude	PA-asym	5	89	1380	Asymmetric control response: R = 0.15%/ms, B_a = 6%, I_a = 1, B_p = 630 W, I_p = 1, $[x_1, x_2, x_3, x_4]$ = [−30, 0, 0, 12]%, A_{min} = 15%, A_{max} = 95%

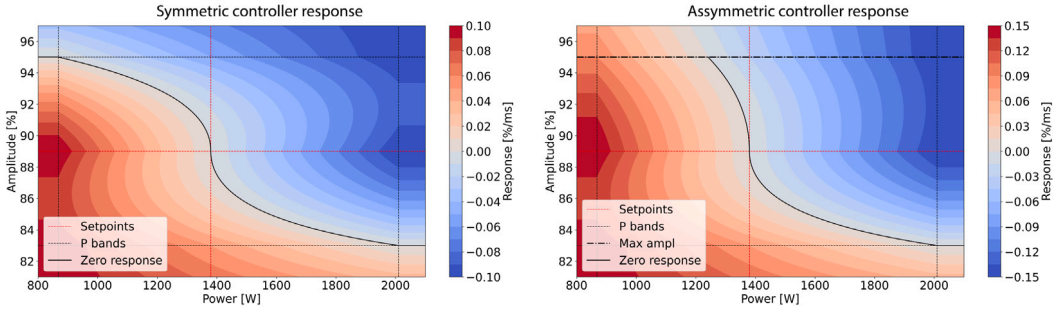


Fig. 10. Combined power-amplitude control response plot of (a) the symmetric and (b) the asymmetric parameter sets used in this study. "P bands" is short for proportional bands and represents the effective bounds of the corresponding parameters B_a and B_p. The black solid line represents where the control method outputs an amplitude change of zero such that the setpoint does not change.

which suggested that low-power conditions could result in underwelding. The control response plots for the symmetric and asymmetric versions are shown in Fig. 10. These plots show the outcome of dA_{PA} presented in Eq. (6) in %/ms over a range of potential power-amplitude combinations. For the asymmetric parameter set, the fuzzy limits were set such that for a decreasing power from the power setpoint, the amplitude is more quickly increased than in the symmetric case, to help prevent underwelding. A_{max} was used to ensure the maximum allowed amplitude setpoint would be the same as for the symmetric case.

To maintain a physical link between combined power-amplitude control and constant amplitude and constant power control, the power proportional band B_p was set to two times the standard deviation of the power observed during constant amplitude control over the full weld length (314 W), resulting in 628 W and subsequently rounded to 630 W. The amplitude proportional band B_a and fuzzy limits were selected such that the amplitude would not exceed the desirable 80%–100% limit, as found with constant power control. Finally, the maximum ramp R was chosen such that the control method could traverse the full amplitude range within 150 ms, which was found from preliminary experiments to be sufficient for a prompt control response. Note: the response scaling factor I reduces the response when the error lies within the proportional band B, allowing for a larger response when the error is far from the setpoint. This scaling was only applied for constant power control and was disabled for combined power-amplitude control by setting $I_a = I_p = 1$. To maintain the same effective maximum ramp R/I within the proportional band, the value used for constant power control ($R = 0.5$, $I_p = 5$) was adjusted to $R = 0.5/5 = 0.1$ for combined power-amplitude control.

Microscopy and mechanical tests

After welding, nine single-lap shear (SLS) coupons with a width of 25 mm were extracted from each weld using the same Compcut ACS 600 equipped with a diamond blade, following the layout shown in Fig. 6. The SLS coupons were tested using a Zwick/Roell 250 kN universal testing machine at a crosshead speed of 1.3 mm/min according to ASTM D1002. Hydraulic grips that were offset to ensure parallel load introduction were used, with an initial grip-to-grip distance of 130 mm. The lap shear strength (LSS) was computed by dividing the maximum force by the measured overlap area. The LSS values presented in this study were compared to those of the one-shot consolidated reference laminate with 24 plies. These reference coupons were slotted single-lap shear specimens with an effective overlap area of 25 mm × 30 mm. The LSS values are reported as a percentage of the average LSS of these reference coupons. This normalization was applied to maintain confidentiality within the consortium in which this study was performed. The use of a one-shot consolidated CF/LMPAEK laminate as the reference enables direct comparison of the relative joint performance obtained in this study. Strength values exceeding 100% therefore indicate that the welded specimens surpassed the average strength of the reference laminate. The normalized LSS is hereafter referred to as strength. After mechanical testing, fractographic microscopy was performed using a Keyence VR-5000 wide-area 3D microscope. From the fracture surface micrographs of T1 to T9, the underwelding percentage was determined for each weld. As illustrated in Fig. 11, the Free Select Tool in GIMP was used to select the underwelded region and the nominal weld area. The pixel counts corresponding to these regions (Px_u and Px_w, respectively) were then obtained using the Histogram tool. The underwelding percentage was subsequently calculated as $\mathrm{Px}_u/\mathrm{Px}_w \times 100\%$.

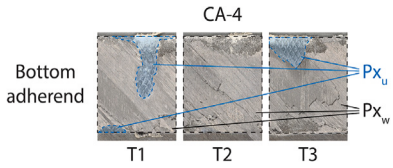


Fig. 11. Example of the procedure used to determine the underwelding percentage, showing the first three coupons of CA-4. The highlighted regions correspond to the underwelded area (Px_u) and the nominal weld area (Px_w).

Results

The generator power and amplitude curves for all welds during welding are shown in Fig. 12. For the welds made with constant

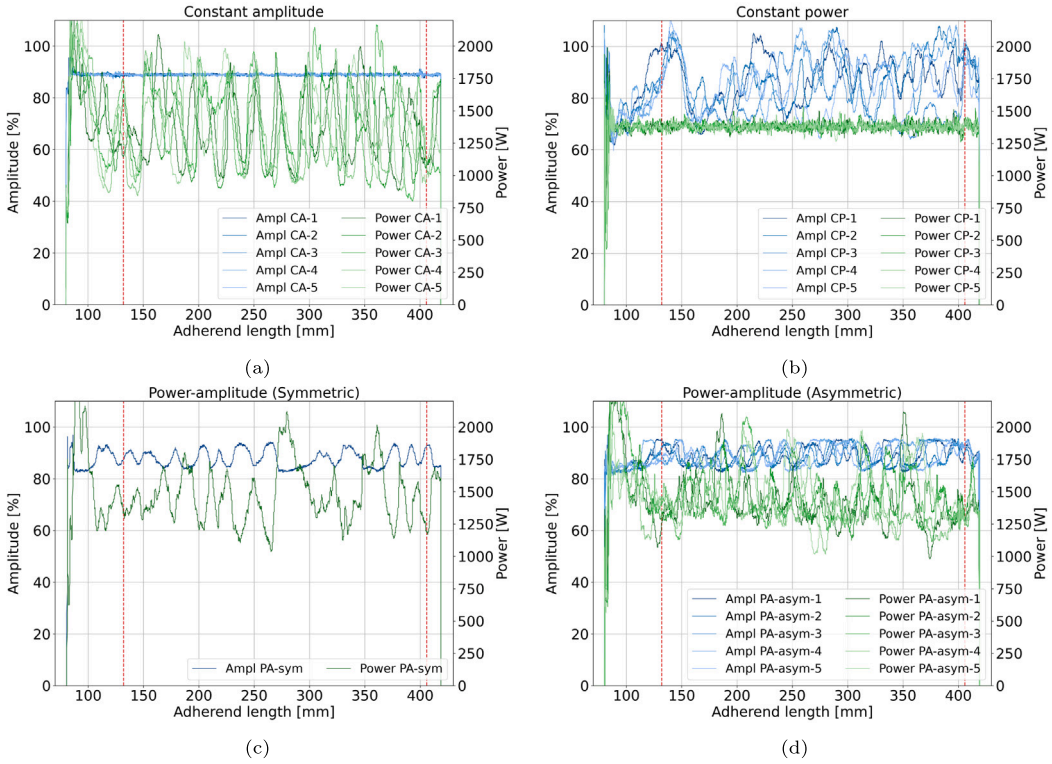


Fig. 12. Power and amplitude curves of the welds made with (a) constant amplitude control, (b) constant power control, (c) symmetric combined power-amplitude control, and (d) asymmetric combined power-amplitude control. The curves have been smoothed using a moving average filter with 20 points. Note: the coupons for mechanical testing were extracted between the distances indicated by the red vertical dashed lines.

amplitude control, it can be seen that the power fluctuates significantly. For the welds made with constant power control, the amplitude fluctuates significantly. For the welds made with symmetric and asymmetric combined power-amplitude control, the amplitude and power fluctuate significantly less.

An overview of the average power and amplitude values for the 16 welds made using the three different control methods is presented in Table 3. Additionally, it gives the average values, standard deviation, and coefficient of variation of all welds together per control method. Welds made using combined power-amplitude control exhibit a lower coefficient of variation in amplitude compared to constant power control, and a lower coefficient of variation in power compared to constant amplitude control.

The strength values of all individual coupons for the various control methods are shown in Fig. 13, together with standard-deviation bands indicating variability around each mean strength. For welds made using the constant amplitude and combined power-amplitude control, the strength exhibits relatively low variability over the weld length, whereas the welds made with constant power control show significantly higher variability. Among the asymmetric power-amplitude welds, two coupons display relatively lower strength, with one being roughly three standard deviations below the average and the other exceeding that threshold; similarly, the constant amplitude welds include two coupons with relatively lower strength, between two and three standard deviations below their average.

An overview of these strength results is provided in Table 4. When considering the average value over five welds for the constant amplitude, constant power, and asymmetric combined power-amplitude control, the welds made with the asymmetric control resulted in the best overall performance with the highest strength. Constant amplitude control yielded welds with a comparable coefficient of variation but a lower strength, while constant power control gave welds with the lowest average strength along with the highest coefficient of variation. The weld made using symmetric combined power-amplitude control performed similarly to the asymmetric combined power-amplitude control welds. Note that these average weld strengths are all higher than the reference strength.

The thermography results are presented in Fig. 14. For the welds made with constant amplitude and asymmetric combined power-amplitude control, it can be seen that the top surface temperature after consolidation is relatively stable over the weld length. However, one of the constant amplitude welds (CA-3) shows a large hot spot at the longitudinal edge at 225 mm with the temperature exceeding 150 °C compared to the average of 96.9 °C. Additionally, one weld made using asymmetric combined power-amplitude control (PA-asym-2) had a small hot spot around 310 mm with a temperature reaching about 130 °C compared to the average of 93.1 °C. For constant power control, the temperatures during welding fluctuate significantly, most notably on weld CP-4, where the temperature is about 80 °C around 240 mm and increases to exceeding the measurement limit of 160 °C at 255 mm, compared to the weld average temperature of 100.8 °C. Furthermore, it can be seen that the hotter and colder spots are seemingly spaced randomly, except for a hot section always occurring near the weld start at about 150 mm.

The fracture surfaces obtained after mechanical testing of representative welds can be seen for all control methods in Fig. 15. The fracture surfaces of the weld made with constant amplitude control in Fig. 15(a) has areas that are underwelded, particularly at the longitudinal edges: the ED did not fully melt and form a strong bond between the adherends indicated by the areas looking more reflective and smooth on both the top and bottom adherends, with often the ED mesh pattern still recognizable. The fracture surfaces of the weld made with constant power control in Fig. 15(b) show the largest areas of underwelding of all control methods: large areas of not fully molten ED can be observed over the entire weld length. These underwelded areas sometimes cover the complete weld width. The fracture surfaces obtained using symmetric combined power-amplitude control in Fig. 15(c) shows several

Table 3
Overview of the average, standard deviation (SD), and coefficient of variation (CoV) of the vibration amplitude and power consumption during welding (respectively, A_w and P_w). For computing these statistics the weld data from the start of T1 to the end of T9 was used, shown in Fig. 6, and indicated by the red vertical dashed lines in Fig. 12.

Controller	Weld No. [–]	$\bar{A}_w$ [%]	A_w SD [%]	A_w CoV [%]	$\bar{P}_w$ [W]	P_w SD [W]	P_w CoV [%]
CA	1	89.0	0.5	0.6	1351	273	20.2
CA	2	89.0	0.5	0.6	1365	293	21.5
CA	3	89.0	0.5	0.6	1396	314	22.5
CA	4	89.0	0.5	0.6	1349	281	20.9
CA	5	89.0	0.5	0.6	1370	295	21.6
CA	Avg. [1–5]	89.0	0.5	0.6	1366	292	21.4
CP	1	87.7	9.2	10.5	1380	29	2.1
CP	2	87.9	9.7	11.1	1380	30	2.2
CP	3	81.1	10.5	12.9	1379	26	1.9
CP	4	89.8	10.2	11.4	1379	29	2.1
CP	5	84.9	9.8	11.5	1380	27	2.0
CP	Avg. [1–5]	86.3	10.3	12.0	1379	28	2.1
PA-sym	1	87.8	3.2	3.7	1471	214	14.6
PA-asym	1	89.4	3.7	4.1	1419	190	13.4
PA-asym	2	88.0	3.3	3.8	1470	164	11.1
PA-asym	3	89.0	3.8	4.2	1438	184	12.8
PA-asym	4	90.8	3.4	3.8	1353	122	9.0
PA-asym	5	88.2	3.9	4.4	1488	218	14.6
PA-asym	Avg. [1–5]	89.1	3.8	4.2	1433	185	12.9

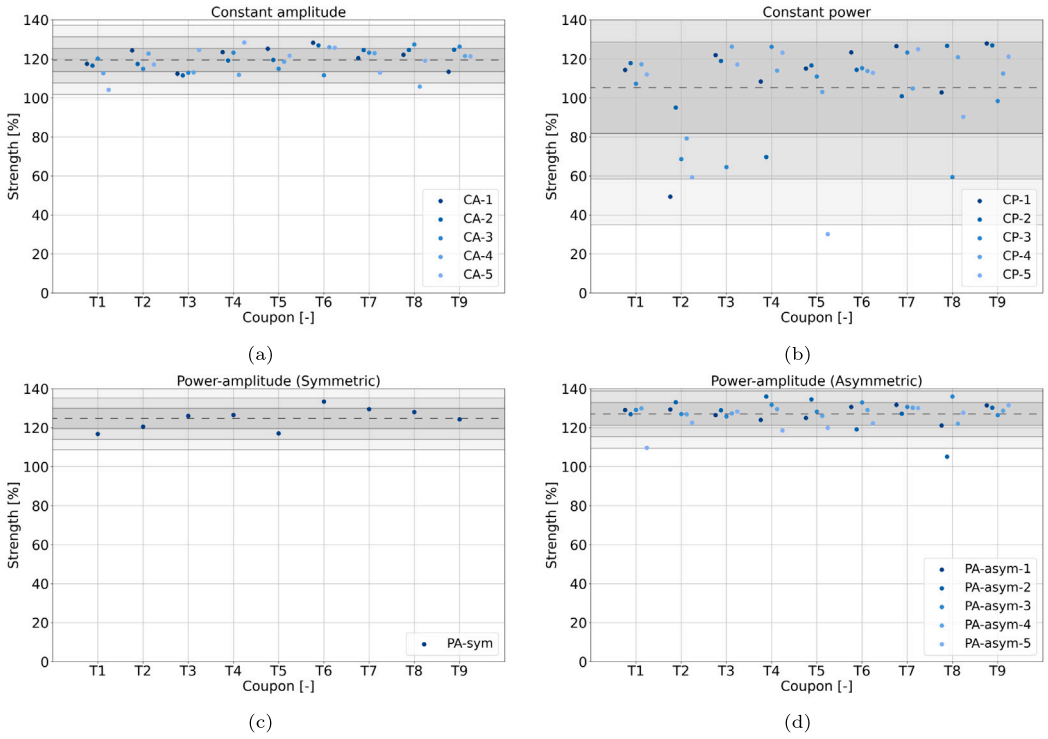


Fig. 13. Strength results of the welds made in this study grouped per coupon number for (a) constant amplitude control, (b) constant power control, (c) symmetric combined power-amplitude control, and (d) asymmetric combined power-amplitude control. The horizontal dashed line represents the average strength of the complete data set, and the first, second, and third grayed areas from this average represent ±1, 2, and 3 standard deviations, respectively.

areas of underwelding. The fracture surfaces obtained with asymmetric combined power-amplitude in Fig. 15(d) shows only one relatively small underwelded area, which is present near the longitudinal edge. Note that for all control methods a similar degree of porosity could be observed at the longitudinal edge.

In Table 5, the underwelding percentage is presented for each weld. The measurements are in line with the qualitative observations from the fracture surfaces in Fig. 15. The underwelding percentage is highest for the constant power control, and lowest for the asymmetric combined power-amplitude control method.

Discussion

With the aim of understanding how to improve the process robustness and weld quality for welding of CF/LMPAEK adherends consisting of unidirectional plies, the present study introduced a novel control method named combined power-amplitude control. We methodically compared this novel method to the state-of-the-art constant amplitude and constant power control methods. The welds produced using these three control methods were evaluated based on their power and amplitude responses, heating uniformity, and resulting weld quality (including lap shear strength and weld uniformity).

Table 4
Overview of strength results (LSS), including average strength, standard deviation (SD), coefficient of variation (CoV), minimum, and maximum.

Controller	Weld No. [–]	Average LSS [%]	SD [%]	CoV [%]	LSS min [%]	LSS max [%]
CA	1	120.8	5.1	4.2	112.4	128.3
CA	2	120.6	4.7	3.9	111.6	127.0
CA	3	119.5	5.6	4.7	111.6	127.4
CA	4	117.3	6.3	5.4	105.8	126.1
CA	5	119.5	6.9	5.8	104.2	128.4
CA	Avg. [1–5]	119.5	5.9	5.0	104.2	128.4
CP	1	110.0	22.8	20.8	49.4	128.0
CP	2	109.7	17.3	15.8	69.7	127.0
CP	3	97.2	24.6	25.3	59.4	126.3
CP	4	110.2	12.9	11.7	79.2	126.3
CP	5	99.1	31.3	31.6	30.2	125.1
CP	Avg. [1–5]	105.2	23.5	22.3	30.2	128.0
PA-sym	1	124.7	5.3	4.3	116.8	133.4
PA-asym	1	127.7	3.5	2.7	121.2	131.7
PA-asym	2	126.8	9.0	7.1	105.2	136.0
PA-asym	3	129.8	3.2	2.4	125.8	136.0
PA-asym	4	127.8	2.4	1.9	122.0	130.3
PA-asym	5	123.4	6.5	5.3	109.7	131.6
PA-asym	Avg. [1–5]	127.1	5.9	4.6	105.2	136.0

Table 5
Underwelding percentage determined from the fracture surfaces of T1 to T9 for all welds.

Weld No. [–]	Underwelding CA [%]	Underwelding CP [%]	Underwelding PA-sym [%]	Underwelding PA-asym [%]
1	3.2	10.5	3.4	1.0
2	4.4	14.4	–	0.6
3	4.6	23.5	–	0.4
4	7.6	10.5	–	1.7
5	5.4	19.6	–	1.1
Avg. [1–5]	5.0	15.7	–	1.0

A key challenge in achieving robust and consistently high weld quality lies in the variability arising during the heating phase. The heating phase of the continuous ultrasonic welding process is highly sensitive to boundary conditions such as tooling, clamping (B. G. Brito et al., 2022; Jongbloed et al., 2021), the material properties (e.g., stiffness), and the local state of the material near the sonotrode (Jongbloed et al., 2020a). All of these factors influence how vibrations are transmitted to the welding interface, determining how much of the input energy is absorbed by the energy director versus how much is dissipated elsewhere in the system and adherends, and they also affect the resulting heat transfer (Fernandez Villegas, 2015; B. G. Brito et al., 2022; Janek et al., 2025). The sensitivity of the welding process to the above-mentioned factors can be substantiated by looking at the equation for viscoelastic heat generation when using constant amplitude control (Eq. (1)). If all mentioned factors were to remain constant during the welding process, an approximately constant power draw from the ultrasonic welding generator would be expected together with a uniform temperature distribution over the length of the welded seam, however, as seen in Figs. 12(a) and 14 this is not the case. This deviation arises because the generator continuously adjusts its power output to maintain a constant amplitude, making the power directly dependent on the mechanical impedance encountered by the sonotrode. The power (Fig. 12(a)) fluctuates very significantly between 800 and 2160 W, and the top surface temperature measured behind the consolidator displays fluctuations between 50 and 125 °C (with one peak above the 160 °C measurement limit) and average of 94.1 °C with an average coefficient of variation (CoV) of 7.9%. The power valleys could be correlated with underwelded areas in the welded seams, as shown in Fig. 16. At these locations, insufficient energy was absorbed by the welding interface to fully melt the energy director and achieve inter-diffusion with the adherends, resulting in the lower-strength coupons observed for this control method. We believe that mainly the boundary conditions like the compactor/consolidator size and location, the clamping, the local variety within the adherends themselves, and the degree of (un)molten material under the sonotrode cause these power fluctuations. Further investigations are needed to understand which factors contribute most to the fluctuations, but this is out of scope for the current study. For the power peaks, a correlation could not clearly be observed.

To avoid power fluctuations altogether, constant power welding could be utilized as explored by Janek et al. (2025). To keep the power constant, the amplitude will have to fluctuate to accommodate changes in the mechanical impedance under the sonotrode. Indeed, for the constant power welds, the amplitude fluctuated significantly as seen in Fig. 12(b). The amplitude fluctuated between 65 and 110% with an average around 86.3% and with coefficient of variation of 12%. It was expected that the peaks and valleys occurring for the amplitude would have an amplified impact on the temperature and weld uniformity compared to peaks and valleys within the power curve. Firstly, because the viscoelastic heating rate (Eq. (1)) is proportional to the square of the cyclic strain imposed on the energy director. Secondly, because a certain minimum vibrational amplitude is expected to be required for the vibrational energy to be transmitted effectively to the energy director. The distribution of the top surface temperature after consolidation, shown in Fig. 14, is consistent with this hypothesis, as large fluctuations in amplitude result in significant variations in heating and, consequently, in temperature (average CoV of 16.7%). Additionally, the amplitude fluctuations, particularly the amplitude valleys, have a significant impact on weld uniformity and strength. As shown in Fig. 17, the valleys correspond to underwelded areas where the energy director was not fully molten, while the amplitude peaks align with areas exhibiting signs of overheating, indicated by porosity and matrix-fiber flow from the top adherend. Among the different control methods, the constant power control method resulted in the largest variation in strength, as observed from Fig. 13 and Table 4. Only this control method exhibited extremely low strength values, which are attributed to underwelded areas, as also observed in Fig. 17 and in

Weld	$\bar{T}$ [°C]	SD [°C]	CoV [%]	Thermography result
CA-1	93.0	6.4	6.9	
CA-2	92.3	5.8	6.3	
CA-3	96.9	9.5	9.8	
CA-4	92.7	6.8	7.3	
CA-5	96.5	7.0	7.3	
CA-[1-5]	94.1	7.5	7.9	
CP-1	96.2	14.6	15.2	
CP-2	94.1	15.3	16.3	
CP-3	90.1	16.1	17.9	
CP-4	100.8	16.4	16.2	
CP-5	94.9	14.4	15.2	
CP-[1-5]	95.2	15.9	16.7	
PA-asym-1	87.8	7.7	8.7	
PA-asym-2	93.1	6.8	7.3	
PA-asym-3	93.6	5.5	5.9	
PA-asym-4	85.5	6.7	7.8	
PA-asym-5	93.9	9.1	9.7	
PA-asym-[1-5]	90.8	8.0	8.8	

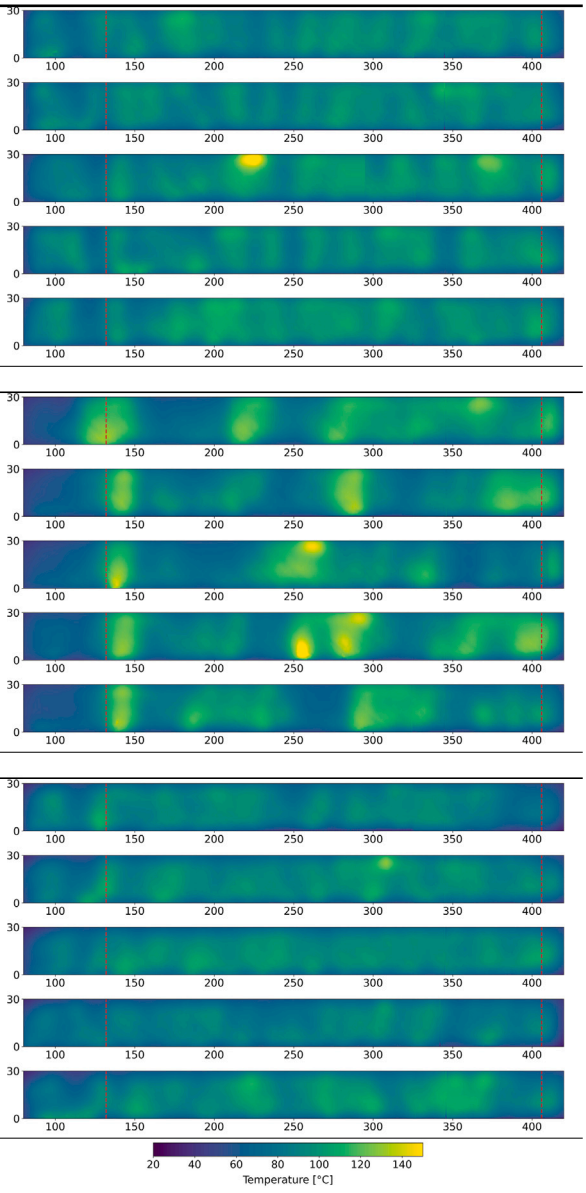


Fig. 14. In-situ thermographic measurements of top surface temperature obtained during welding, including average temperature ($\bar{T}$), standard deviation (SD), and coefficient of variation (CoV) for the constant amplitude, constant power, and asymmetric combined power-amplitude control methods. For computing these statistics, the data from the start of T1 to the end of T9 was used as seen in Fig. 6, which is indicated in this figure by the red vertical dashed lines, and a margin of 3 mm was excluded from both longitudinal weld edges. The axes adherend dimensions are in mm.

Table 5. The selected power setpoint of 1380 W also produced coupons with strength values and fracture surfaces comparable to those obtained using constant amplitude control and was therefore considered a fair power setpoint baseline. However, considerable variability in weld quality remained. Since both high-quality and severely underwelded specimens were obtained at the same setpoint, the observed variability appears to be associated with the constant power control strategy rather than solely with the setpoint selection.

As discussed, significant fluctuations in power and amplitude have negative implications for the weld uniformity and should be avoided. However, because they are so strongly correlated, the only possibility to achieve this is to control both and allow both parameters to fluctuate, but ensure that the fluctuations of both parameters are minimized. By minimizing the fluctuations, we mean preventing the occurrence of maximum and minimum values linked to overheating and underwelding, respectively. We have shown this with our combined power-amplitude control method. Fig. 12(c) (symmetrical fuzzy limits) and Fig. 12(d) (asymmetric fuzzy limits) show that indeed for combined power-amplitude control the power and amplitude fluctuate considerably less compared to pure constant amplitude (Fig. 12(a)) or constant power control (Fig. 12(b)) methods. This is further substantiated by the calculated coefficients of variation of the power and amplitude data in Table 3. For the symmetrical and asymmetric power-amplitude welds an average coefficient of variation in power (P) and amplitude (A) of, respectively, 14.6% (P) and 3.7% (A), and 12.9% (P) and 4.2% (A) was observed, while for constant amplitude and constant power welds this was, respectively, 21.4% (P) and 12.0% (A). This is a 40% reduction in power fluctuation and a 65% reduction in amplitude fluctuation when comparing the results of the asymmetric combined power-amplitude welds to the constant amplitude and constant power

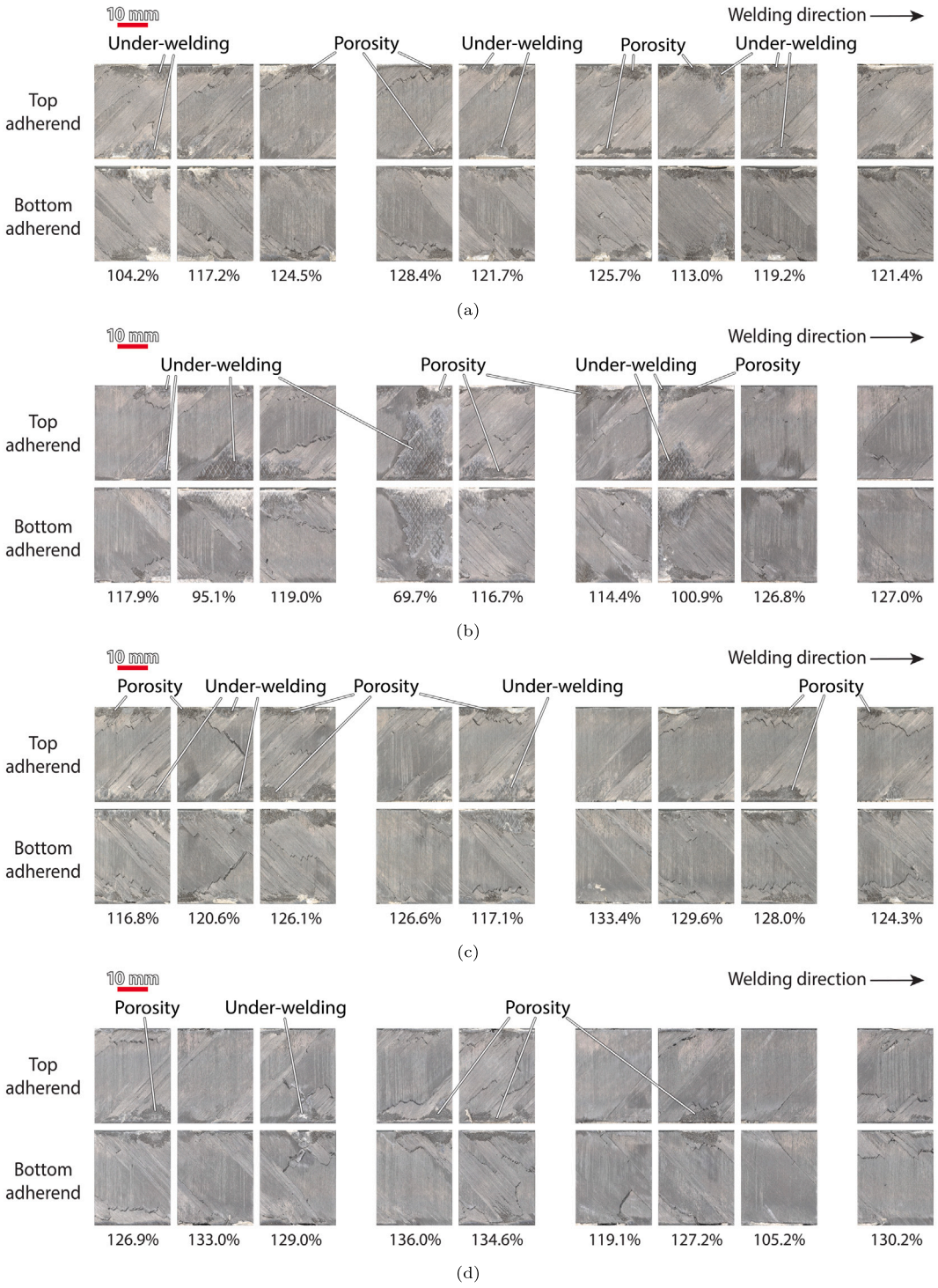


Fig. 15. Fracture surfaces of all tested coupons for four representative welds: (a) constant amplitude control (CA-5), (b) constant power control (CP-2), (c) symmetric combined power-amplitude control (PA-sym), and (d) asymmetric combined power-amplitude control (PA-asym-2). The coupons are spaced as they were extracted from the weld as shown in Fig. 6. The strength of each coupon is included.

control methods. These lower power and amplitude fluctuations result in a more uniform top surface temperature distribution, particularly compared to the constant power control method as seen in Fig. 14, given the lower coefficient of variation of 8.8% as compared to 16.7%, while being comparable to the uniformity of constant amplitude control with a coefficient of variation of 7.9%.

Combined power-amplitude control resulted in 6.4% higher weld strength at a comparable coefficient of variation compared to constant amplitude welding. This difference was found to be statistically significant according to a two-tailed Welch's t-test of the average strengths of the five constant amplitude control welds and the five combined power-amplitude control welds ($p = 5.88 \times 10^{-4}$). The increase in strength is likely attributed to the reduction in underwelded area of about 80% (Table 5) compared to the welds made using the constant amplitude control method. Furthermore, the combined power-amplitude welds resulted in a 20.8% higher strength compared to constant power welding, while reducing the coefficient of variation from 22.3% to 4.6%. Two coupons from the welds made using the

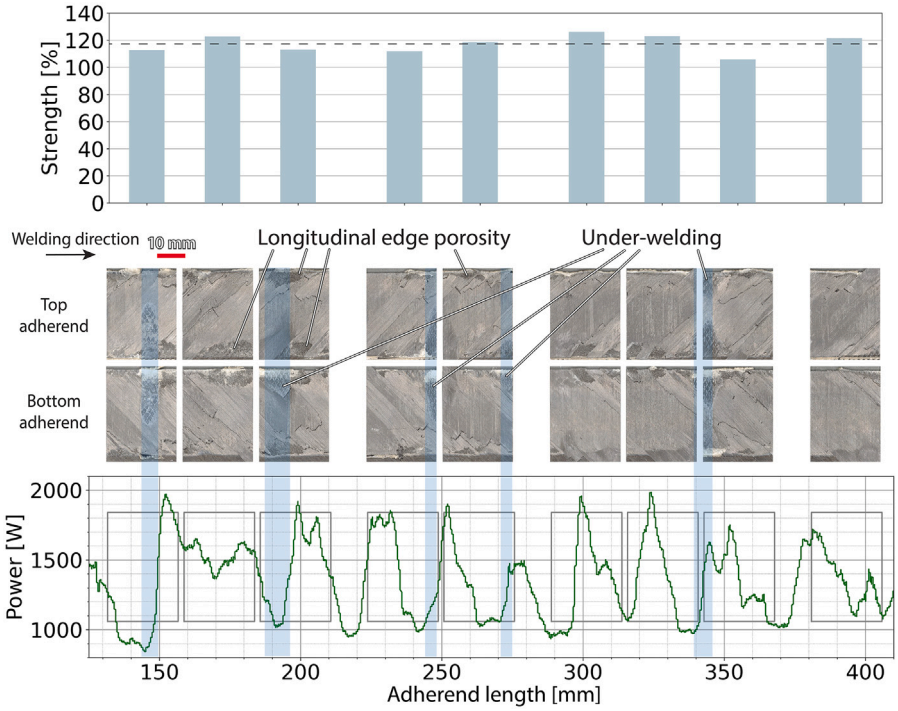


Fig. 16. Representative example of strength results, fractography, and corresponding weld power data for constant amplitude weld CA-4. Power valleys (blue) correspond to underwelded sections that are typically linked to lower strength.

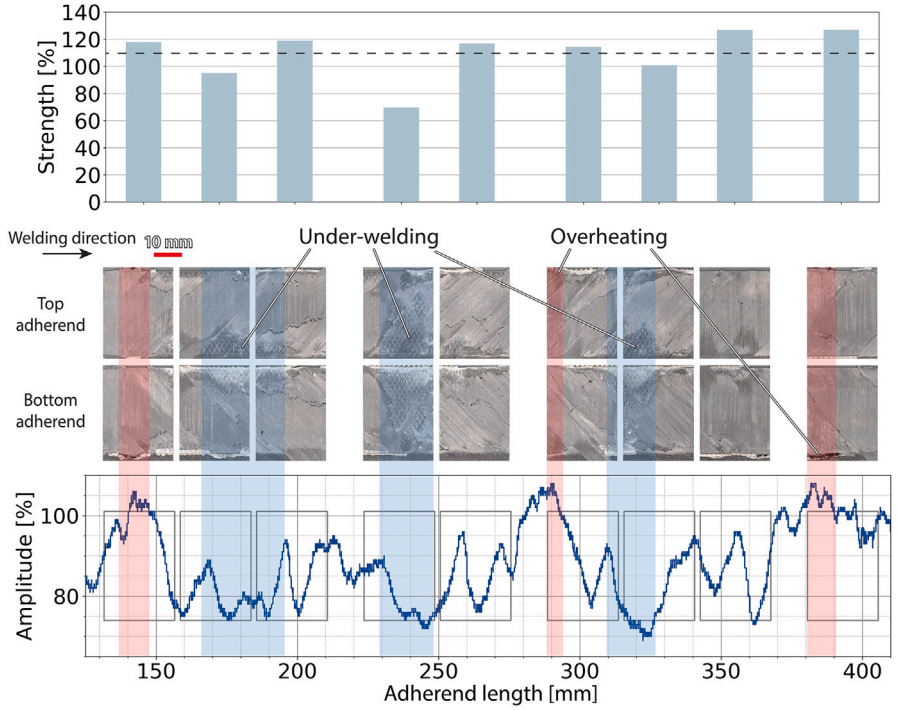


Fig. 17. Representative example of strength results, fractography, and corresponding weld amplitude data for constant power weld CP-2. Amplitude valleys lower than 80% (blue) correspond to underwelded sections and low strength, and above 100% (red) to overheated sections.

asymmetric power-amplitude control method showed relatively lower strengths of 105.2% and 109.7%, compared to the average normalized strength of 127.1% as seen in Fig. 13(d). The coupon with a strength of 105.2% is considered an outlier, falling outside 3 standard deviations from the average as seen in Fig. 13(d), according to the 3σ-rule. The fracture surface (Fig. 18(a)) shows a very clean fracture between the first and second ply of the top adherend without any visible porosity, underwelding or overwelding, making it challenging to identify the cause of the low strength. Most likely the low strength originates from low interlaminar ply adhesion, either from an existing delamination or

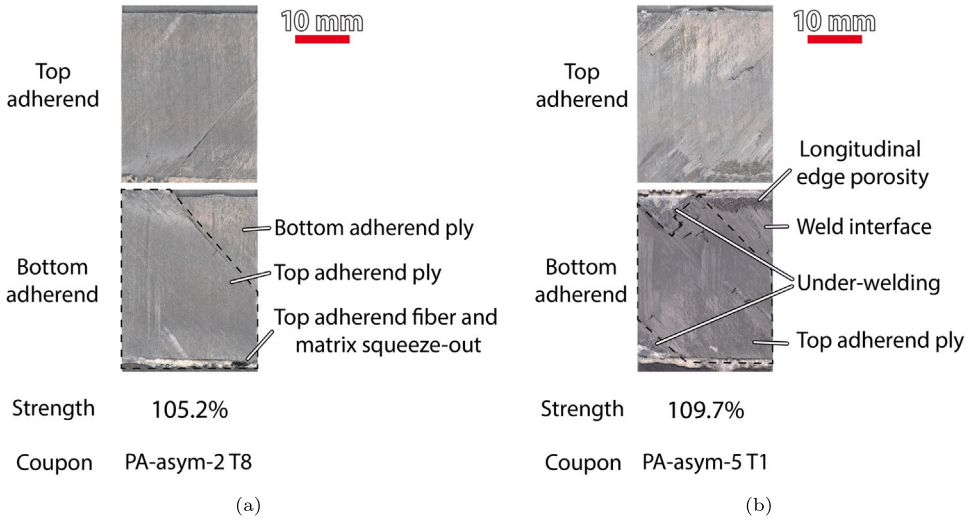


Fig. 18. Fractographic images of the two lowest-strength coupons after mechanical testing, welded using combined power-amplitude control with asymmetric fuzzy limits.

matrix poor area locally within the top adherend. For the coupon with a strength of 109.7% likely the cause was local insufficient heating, indicated by some not fully molten energy director material as seen in the fracture surface (Fig. 18(b)) on both longitudinal edges, effectively lowering the welded area. Still falling within 3 standard deviations from the mean, this strength value was not considered an outlier. Moreover, combined power-amplitude control was not able to eliminate the porosity observed near the longitudinal edges of the weld, with the effect being present for all investigated control methods, as shown in Fig. 15. The porosity appeared similar in all cases, both in morphology and location, suggesting that the cause is most likely not related to the control method.

Note that in this study, strength values exceeding 100% were observed, indicating that the weld strength surpassed that of the one-shot consolidated reference samples. The underlying cause is likely twofold. First, the presence of a resin-rich weld interface, with a thickness of approximately 0.26 mm, provides a more compliant interlayer capable of plastic deformation. This allows for stress redistribution across the interface despite the increased secondary bending, reducing peak shear stress concentrations and thereby increasing the strength compared to the one-shot consolidated reference coupons, which effectively had a weld line thickness of 0.00 mm. Second, resin flash originating from the energy director likely contributed to a reduction in peak peel stresses by forming a fillet along the longitudinal edges of the welds, further enhancing the overall load-bearing capacity of the welded joints. The normalized strength values obtained in the present study are consistent with the high weld performance reported in a previous CF/LMPAEK ultrasonic welding study (Köhler et al., 2024), where joint strengths approaching or exceeding the strength of the reference laminate have also been observed.

Asymmetric fuzzy limits were implemented to reduce the likelihood of low-power values, as the preliminary experiment using symmetric fuzzy limits still exhibited underwelded areas, as shown in Fig. 15(c) and Table 5. In light of observations from constant amplitude welding, where power valleys were associated with underwelded areas, the need to avoid such conditions is well justified. To further reduce this likelihood, the maximum ramp parameter was increased for the final asymmetric parameter set, allowing the system to respond more quickly to eliminate power and amplitude errors. It should be noted that the increase in the maximum ramp parameter primarily enhances the responsiveness of the control system rather than altering the target power-amplitude combinations themselves. As such, while it facilitates faster correction of undesirable states, the reduction in underwelded areas is attributed to the combined effect of the asymmetric limits and improved dynamic response, rather than to the ramp increase.

The combined power-amplitude control method demonstrates an improvement over constant amplitude welding in terms of weld quality under the conditions investigated in this study. Although both methods exhibit a similar coefficient of variation in the measured top surface temperature (Fig. 14), the combined power-amplitude control method results in a higher average lap shear strength (Fig. 13, Table 4) and fewer underwelded areas (Fig. 15, Table 5). This discrepancy suggests that the temperature measured at the top surface of the top adherend does not fully capture the thermal conditions at the welding interface. It should be noted that the welding interface temperature is the dominant temperature governing joint formation. The measured top-surface temperature is a consequence of the welding interface temperature, resulting from heat transfer from the welding interface to the upper surface of the top adherend, as well as viscoelastic through-thickness heating within the top adherend (Jongbloed et al., 2021). In particular, it is likely that the actual temperature distribution at the interface is less uniform for constant amplitude welding. This is substantiated by the presence of underwelded areas (Fig. 15(a)), which indicate locally lower temperatures that were not reflected in the surface measurements. Such local temperature variations at the interface may not be captured by top surface thermography due to heat redistribution as thermal energy propagates through the thickness of the top adherend. Consequently, small regions of insufficient heating can be masked, leading to an underestimation of the true thermal non-uniformity. In contrast, the combined power-amplitude control strategy mitigates these local deficiencies by dynamically adjusting both parameters, resulting in more heating at the welding interface and improved weld quality.

Conclusion

This study investigated the improvement of process robustness and weld quality in continuous ultrasonic welding of CF/LMPAEK adherends made from unidirectional plies by introducing a novel combined power-amplitude control method. The results obtained under the conditions investigated in this study indicate that this control method improves weld quality relative to conventional constant amplitude welding and the more recently introduced constant power control method, yielding higher average lap shear strength, reduced scatter, fewer underwelded areas, and more uniform welds. These conclusions are supported by the following key findings:

- Under constant-amplitude control, pronounced power fluctuations were observed, with power valleys correlating with underwelded regions. No consistent evidence of overheating was associated with power peaks within the present study.
- Under constant-power control, amplitude fluctuations were significant, with amplitude valleys and peaks producing underwelded and overheated regions, respectively.
- Amplitude fluctuations exhibited a greater detrimental influence on weld strength and weld uniformity than power fluctuations under the control conditions investigated in this study.
- The combined power-amplitude control method reduces extreme fluctuations in both amplitude and power.
- Temperature measurements indicated that constant-amplitude and combined power-amplitude control yielded comparable top-surface temperature uniformity after consolidation, whereas constant-power control resulted in a more non-uniform temperature distribution. However, the top surface temperature measurements likely do not fully capture the temperature distribution at the welding interface, as evidenced by the larger number of underwelded areas observed for constant amplitude control compared to combined power-amplitude control.
- Observations made during implementation of the combined control method suggested symmetric fuzzy limits may not adequately prevent low-power conditions that could result in underwelding, motivating the use of asymmetric limits.

Collectively, these findings indicate that combined power-amplitude control represents a promising approach for continuous ultrasonic welding of thermoplastic composites. Under the processing conditions investigated in this study, the method led to improved weld strength, weld uniformity, and a reduction in underwelded and overheated regions. These results demonstrate the potential of the control strategy to improve process robustness. Assessing parameter transferability across different materials and configurations represents an important next step toward broader implementation of the approach. Additionally, the relationship between measured top-surface temperatures and the actual thermal conditions at the welding interface requires further investigation. Further optimization of the control parameters may yield additional improvements and strengthen the applicability of the approach for high-performance composite joining applications.

CRediT authorship contribution statement

Nigel van Nierop: Writing – review & editing, Writing – original draft, Visualization, Validation, Methodology, Investigation, Formal analysis, Conceptualization. **Bram Jongbloed:** Writing – review & editing, Writing – original draft, Validation, Supervision, Project administration, Methodology, Investigation, Funding acquisition, Conceptualization.

Declaration of generative AI and AI-assisted technologies in the manuscript preparation process

During the preparation of this work the author(s) used Copilot and ChatGPT in order to improve readability of certain paragraphs. After using this tool/service, the author(s) reviewed and edited the content as needed and take(s) full responsibility for the content of the published article.

Declaration of competing interest

The authors declare that they have no known competing financial interests or personal relationships that could have appeared to influence the work reported in this paper.

Acknowledgments

This research was funded by the Netherlands Enterprise Agency (RVO) within the scope of the Aerofusion project of the National Growth Fund Aviation in Transition supporting research (Groeifonds Luchtvaart in Transitie ondersteunend onderzoek) with grant number [LITO&O24-03724744]. The authors thank dr. Irene Fernandez Villegas for her advice in the conceptualization phase of the research and for reviewing this paper and the authors thank Toray Advanced Composites for providing the material used for this work. Furthermore, the authors thank Berthil Grashof for significantly contributing to the development of the control methods used in this study and for his technical support. A patent application related to the findings of this work on combined power-amplitude control has been filed on 5 March 2026.

Data availability

Data are contained within the article.

References

Asnani, C., 2025. The Effect of the Adherends' Thickness on Continuous Ultrasonic Welding of Thermoplastic Composites TU Delft repository MSc thesis. doi:https://resolver.tudelft.nl/uuid:12dab1e9-8796-4faf-983f-ab7c4a507d99.

B. G. Brito, C., Teuwen, J.J.E., Dransfeld, C.A., Fernandez Villegas, I., 2022. The effects of misaligned adherends on static ultrasonic welding of thermoplastic composites. Composites A 155, 106810. http://dx.doi.org/10.1016/j.compositesa.2022.106810.

Benatar, A., Eswaran, R.V., Nayar, S.K., 1989. Ultrasonic welding of thermoplastics in the near-field. Polym. Eng. Sci. 29 (23), 1689–1698. http://dx.doi.org/10.1002/pen.760292311.

Benatar, A., Gutowski, T.G., 1989. Ultrasonic welding of PEEK graphite APC-2 composites. Polym. Eng. Sci. 29 (23), 1705–1721. http://dx.doi.org/10.1002/pen.760292313.

Choudhary, A., Bîrgăoanu-Acăei, I., Fernandez Villegas, I., 2026. Robotic sequential ultrasonic welding of thermoplastic composites: From coupons to a full-scale fuselage demonstrator. Process 14 (3), 528. http://dx.doi.org/10.3390/pr14030528.

Costa, A., Botelho, E., Costa, M., Narita, N., Tarpani, J., 2012. A review of welding technologies for thermoplastic composites in aerospace applications. J. Aerosp. Technol. Manag. 4, 255–266. http://dx.doi.org/10.5028/jatm.2012.040303912.

Fernandez Villegas, I., 2014. Strength development versus process data in ultrasonic welding of thermoplastic composites with flat energy directors and its application to the definition of optimum processing parameters. Composites A 65, 27–37. http://dx.doi.org/10.1016/j.compositesa.2014.05.019.

Fernandez Villegas, I., 2015. In situ monitoring of ultrasonic welding of thermoplastic composites through power and displacement data. J. Thermoplast. Compos. Mater. 28 (1), 66–85. http://dx.doi.org/10.1177/0892705712475015.

Fernandez Villegas, I., 2019. Ultrasonic welding of thermoplastic composites. Front. Mater 6, 291. http://dx.doi.org/10.3389/fmats.2019.00291.

Fernandez Villegas, I., Moser, L., Yousefpour, A., Mitschang, P., Bersee, H.E., 2013. Process and performance evaluation of ultrasonic, induction and resistance welding of advanced thermoplastic composites. J. Thermoplast. Compos. Mater. 26 (8), 1007–1024. http://dx.doi.org/10.1177/0892705712456031.

Gardiner, G., 2006. Thermoplastic composites gain leading edge on the A380. https://www.compositesworld.com/articles/thermoplastic-composites-gain-leading-edge-on-the-a380, (Accessed 01 March 2026).

Gardiner, G., 2022. Thermoplastic composites welding advances for more sustainable airframes. https://www.compositesworld.com/articles/thermoplastic-composites-welding-advances-for-more-sustainable-airframes, (Accessed 01 March 2026).

Janek, M., Görick, D., Larsen, L., Jarka, S., Kupke, M., 2025. Investigation of power and amplitude control in continuous ultrasonic welding of unidirectional CFRPs: A comparative study. Composites A 199, 109194. http://dx.doi.org/10.1016/j.compositesa.2025.109194.

Jongbloed, B.C.P., Asfew, K.N., Teuwen, J.J.E., Peeters, D.M.J., 2024. The challenges with fast heating rates in the processing of thermoplastic composites. In: Proceedings of the International Conference and Exhibition on Thermoplastic Composites. ITHEC.

Jongbloed, B.C.P., Teuwen, J.J.E., Benedictus, R., Fernandez Villegas, I., 2020a. On differences and similarities between static and continuous ultrasonic welding of thermoplastic composites. Composites B 203, 108466. http://dx.doi.org/10.1016/j.compositesb.2020.108466.

Jongbloed, B.C.P., Teuwen, J.J.E., Benedictus, R., Fernandez Villegas, I., 2021. A study on through-the-thickness heating in continuous ultrasonic welding of thermoplastic composites. Mater 14 (21), 6620. http://dx.doi.org/10.3390/ma14216620.

Jongbloed, B.C.P., Teuwen, J.J.E., Fernandez Villegas, I., 2023. On the use of a rounded sonotrode for the welding of thermoplastic composites. J. Adv. Join Process. 7, 100144. http://dx.doi.org/10.1016/j.jajp.2023.100144.

Jongbloed, B.C.P., Teuwen, J.J.E., Palardy, G., Fernandez Villegas, I., Benedictus, R., 2020b. Continuous ultrasonic welding of thermoplastic composites: Enhancing the weld uniformity by changing the energy director. J. Compos. Mater. 54 (15), 2023–2035. http://dx.doi.org/10.1177/0021998319890405.

Jongbloed, B.C.P., Vinod, R., Teuwen, J., Benedictus, R., Fernandez Villegas, I., 2022. Improving the quality of continuous ultrasonically welded thermoplastic composite joints by adding a consolidator to the welding setup. Composites A 155, 106808. http://dx.doi.org/10.1016/j.compositesa.2022.106808.

Köhler, F., Fernandez Villegas, I., Dransfeld, C., Herrmann, A., 2024. On the influence of welding parameters and their interdependence during robotic continuous ultrasonic welding of carbon fibre reinforced thermoplastics. Mater 17 (21), 5282. http://dx.doi.org/10.3390/ma17215282.

Larsen, L., Endrass, M., Jarka, S., Bauer, S., Janek, M., 2025. Exploring ultrasonic and resistance welding for thermoplastic composite structures: Process development and application potential. Composites B 289, 111927. http://dx.doi.org/10.1016/j.compositesb.2024.111927.

Liu, J., Quan, D., Scarselli, G., Alderliesten, R., Wang, H., Zhao, G., 2025. Developments and future prospects of welding technology for carbon fiber thermoplastic composites. Composites B 297, http://dx.doi.org/10.1016/j.compositesb.2025.112314.

Offringa, A., 2010. New thermoplastic composite design concepts and their automated manufacture. JEC Compos. Mag. 58, 45–49.

Palardy, G., Fernandez Villegas, I., 2017. On the effect of flat energy directors thickness on heat generation during ultrasonic welding of thermoplastic composites. Compos. Interfaces 24 (2), 203–214. http://dx.doi.org/10.1080/09276440.2016.1199149.

Potente, H., 1984. Ultrasonic welding — Principles & theory. Mater. Des. 5 (5), 228–234. http://dx.doi.org/10.1016/0261-3069(84)90032-3.

Senders, F., van Beurden, M., Palardy, G., Fernandez Villegas, I., 2016. Zero-flow: A novel approach to continuous ultrasonic welding of CF/PPS thermoplastic composite plates. Adv. Manuf.: Polym. Compos. Sci. 2 (3–4), 83–92. http://dx.doi.org/10.1080/20550340.2016.1253968.

van Stuyvesant Meijen, J.M., Jongbloed, B.C.P., 2025. Assessing weld quality in continuous ultrasonic welding of thermoplastic composites via in-situ monitoring. In: Proceedings of the SAMPE Europe Conference 2025. Vol. SAMPE Europe Conference.

van Dooren, K., Bisagni, C., 2023. Design, analysis and testing of thermoplastic welded stiffened panels to investigate skin-stringer separation in post-buckling. Composites B 267, 111033. http://dx.doi.org/10.1016/j.compositesb.2023.111033.

Yuan, J., Xiao, H., Wang, Y., Cui, W., Duan, Y., Xin, Z., Wang, B., 2026. Ultrasonic welding process and strategies for performance regulation of Fiber reinforced thermoplastic composites: A review. J. Manuf. Process. 157, 531–553. http://dx.doi.org/10.1016/j.jmapro.2025.11.084.

Zhang, Z., Wang, X., Luo, Y., Zhang, Z., Wang, L., 2010. Study on heating process of ultrasonic welding for thermoplastics. J. Thermoplast. Compos. Mater. 23 (5), 647–664. http://dx.doi.org/10.1177/0892705709356493.

Zhao, T., Palardy, G., Fernandez Villegas, I., Rans, C., Martinez, M., Benedictus, R., 2017. Mechanical behaviour of thermoplastic composites spot-welded and mechanically fastened joints: A preliminary comparison. Composites B 112, 224–234. http://dx.doi.org/10.1016/j.compositesb.2016.12.028.